BIOLOGICAL CRYSTALLOGRAPHY

ISSN 1399-0047

The structure of apo ArnA features an unexpected central binding pocket and provides an explanation for enzymatic cooperativity

Utz Fischer, Simon Hertlein and Clemens Grimm*

Department of Biochemistry, Biocenter of the University of Würzburg, Am Hubland, 97074 Würzburg, Germany. *Correspondence e-mail: clemens.grimm@uni-wuerzburg.de

Received 10 October 2014
Accepted 4 December 2014

Keywords: ArnA.

PDB reference: full-length apo ArnA, 4wkg

Supporting information: this article has supporting information at journals.iucr.org/d

The bacterial protein ArnA is an essential enzyme in the pathway leading to the modification of lipid A with the pentose sugar 4-amino-4-deoxy-L-arabinose. This modification confers resistance to polymyxins, which are antibiotics that are used as a last resort to treat infections with multiple drug-resistant Gram-negative bacteria. ArnA contains two domains with distinct catalytic functions: a dehydrogenase domain and a transformylase domain. The protein forms homohexamers organized as a dimer of trimers. Here, the crystal structure of apo ArnA is presented and compared with its ATP- and UDP-glucuronic acid-bound counterparts. The comparison reveals major structural rearrangements in the dehydrogenase domain that lead to the formation of a previously unobserved binding pocket at the centre of each ArnA trimer in its apo state. In the crystal structure, this pocket is occupied by a DTT molecule. It is shown that formation of the pocket is linked to a cascade of structural rearrangements that emerge from the NAD^+-binding site. Based on these findings, a small effector molecule is postulated that binds to the central pocket and modulates the catalytic properties of ArnA. Furthermore, the discovered conformational changes provide a mechanistic explanation for the strong cooperative effect recently reported for the ArnA dehydrogenase function.

1. Introduction

Cationic antimicrobial peptides (CAMPs) act on the outer membrane of Gram-negative bacteria by the displacement of the calcium and magnesium ions that bridge the negatively charged phosphosugars of lipopolysaccharides (LPS). The damage (Lounatmaa & Nanninga, 1976; Lounatmaa *et al.*, 1976) induced by this mechanism enables the access of further molecules from the exterior (Hancock *et al.*, 1995; Zasloff, 2002). Once CAMPs have gained access to the periplasm, they integrate into the cytoplasmic membrane, where they induce pore formation (Matsuzaki, 1999; Shai, 1999; Yang *et al.*, 2000). Remarkably, the acquisition of resistance by a bacterial strain sensitive towards CAMPs is comparably improbable (Reddy *et al.*, 2004; Zasloff, 2002). The increasing spread of multiple drug-resistant (MDR) Gram-negative strains has triggered a renaissance of several antibiotics whose clinical use had been widely abandoned decades ago owing to their toxic side effects. Polymyxins, which are antibiotics belonging to the CAMP family, are currently used as a last resort to treat infections with Gram-negative MDR strains including those from the genera *Pseudomonas*, *Acinetobacter*, *Salmonella* and *Klebsiella* (Li *et al.*, 2006; Vaara, 2013; Yahav *et al.*, 2012; Zavascki *et al.*, 2007). Polymyxins target the bacterial outer membrane by binding to the lipid A moiety of LPS. Thus, the

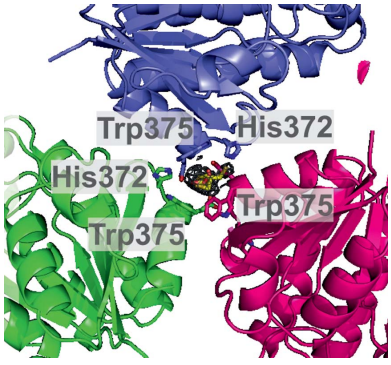

main resistance mechanism of Gram-negative bacteria against this group of antibiotics involves modification (Falagas *et al.*, 2010; Velkov *et al.*, 2010; Gunn, 2001; Guo *et al.*, 1997) or even complete loss (Moffatt *et al.*, 2010) of lipid A. A modification that is frequently found in polymyxin-resistant strains of Gram-negative bacteria is the addition of the positively charged pentose 4-amino-4-deoxy-L-arabinose (Ara4N) to lipid A (Nummila *et al.*, 1995; Helander *et al.*, 1994; Guo *et al.*, 1997; Gunn *et al.*, 1998; Zhou *et al.*, 2001; Trent *et al.*, 2001; Gunn, 2001) catalysed by the gene products of the *pmrHFIJKLM* operon and the *pmrE* gene (Gunn, 2001; Breazeale *et al.*, 2002, 2003, 2005); see Fig. 1(*a*) for an overview of the pathway. The pathway starts with the oxidation of UDP-glucose to UDP-glucuronic acid (UGA) by UDP-glucose-6-dehydrogenase (Ugd; Rocha *et al.*, 2011). The first enzyme specific for the Ara4N modification is ArnA, a protein containing two domains with two distinct enzymatic functions. Its C-terminal domain possesses an extended short-chain dehydrogenase/reductase fold (Kallberg *et al.*, 2010; Kavanagh *et al.*, 2008; Eixelsberger *et al.*, 2012) and catalyses the NAD^+-dependent oxidative decarboxylation of UDP-glucuronic acid (UGA) to UDP-4-keto-xylose (UX4O; Gatzeva-Topalova *et al.*, 2004). In the second step of the pathway, ArnB catalyses the transamination of UX4O to UDP-L-Ara4N (UX4N) with

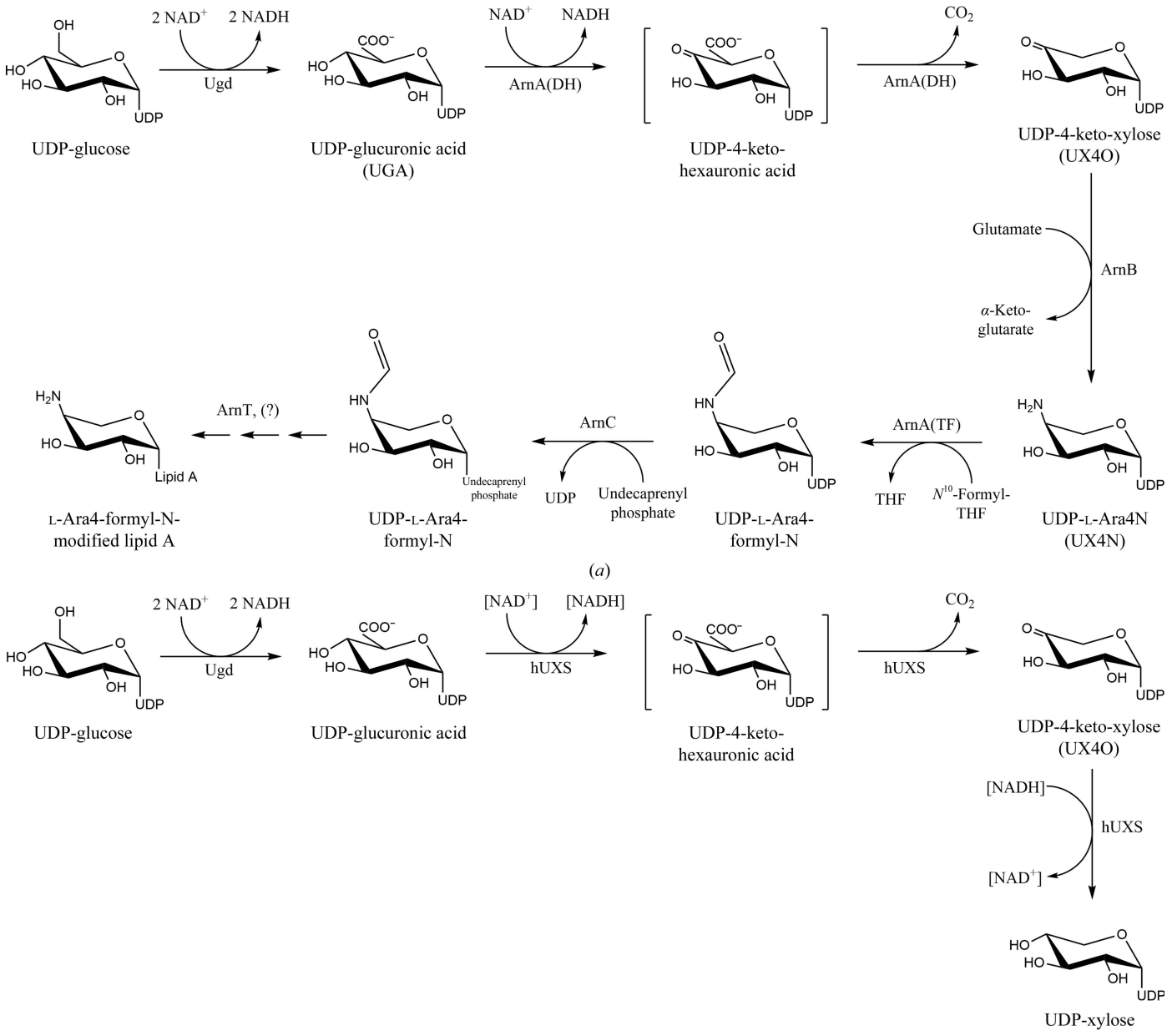

Figure 1
(*a*) Proposed pathway for the 4-amino-4-deoxy-L-arabinose modification of lipid A. (*b*) Reaction catalysed by the human ArnA orthologue UDP-α-D-xylose synthase (hUXS). In contrast to ArnA, hUXS does not release the reduced nucleotide cofactor but rather transfers the reducing equivalents yielded in the first reaction step back onto the substrate. Therefore, the primary reaction product of hUXS is UDP-xylose. Abbreviations: Ugd, UDP-glucose-6-dehydrogenase.

glutamate as the amino-group donor. In the third step, the UX4N amino group is formylated to UDP-L-Ara4-formyl-N in an N^{10}-formyltetrahydrofolate-dependent reaction catalysed by the N-terminal domain of ArnA. Of note, both domains of ArnA can be expressed separately without the loss of their respective enzymatic activity (Gatzeva-Topalova *et al.*, 2005*a*). ArnC then transfers the L-Ara4-formyl-N moiety from UDP onto undecaprenyl phosphate, which anchors the modified sugar in the inner membrane (Breazeale *et al.*, 2005). After transition to the periplasm, the L-Ara4-formyl-N moiety is finally transferred onto lipid A in a reaction catalysed by ArnT, an enzyme of the inner membrane (Trent *et al.*, 2001). All enzymes of the pathway are highly conserved in Gram-negative bacteria and are necessary for the L-Ara4-formyl-N modification of lipid A (Gunn *et al.*, 2000). This makes them highly attractive targets for the design of novel compounds for the treatment of infections with polymyxin-resistant, Gram-negative MDR bacteria. Crystal structures that allow insight into the respective mode of action of individual components of the pathway are available for Ugd (Rocha *et al.*, 2011; Chen *et al.*, 2011), ArnB (Lee & Sousa, 2014; Noland *et al.*, 2002) and, in particular, ArnA. For the latter, the transformylase (TF) domain (Gatzeva-Topalova *et al.*, 2005*a*) and the dehydrogenase (DH) domain (Gatzeva-Topalova *et al.*, 2004) have been crystallized separately, as well as the full-length enzyme (Gatzeva-Topalova *et al.*, 2005*b*). The crystal structure of full-length ArnA appears as a dimer of trimers arranged in two coaxially stacked, three-bladed propellers. This is consistent with data from size-exclusion chromatography and multi-angle light-scattering analysis that suggest a stable hexameric oligomerization state regardless of the presence or absence of substrates (Gatzeva-Topalova *et al.*, 2005*b*). In contrast, the individually expressed TF and DH domains do not form hexamers in solution and appear as monomers in the respective crystal structures (Gatzeva-Topalova *et al.*, 2005*b*). The structures of full-length ArnA available to date are based on crystals grown in the presence of UGA and the NAD^+ analogue ATP. Gatzeva-Topalova and coworkers observed distinct electron density for the two small molecules bound within a deep cleft on the DH domain. We will therefore refer to this structure as the 'substrate-bound' form. A superposition of the structure of the substrate-bound DH domain from full-length ArnA with the substrate-free structure of the individually overexpressed DH domain indicates major structural rearrangements in the vicinity of the binding sites. This includes, among other rearrangements, a loop that blocks the NAD^+-binding site in the apoenzyme and which is displaced more than 10 Å to form a small helix trapping the UGA molecule in the substrate-bound structure. Here, we present the crystal structure of full-length ArnA in its apo state. While the fundamental architecture, domain organization and oligomerization interfaces remain unchanged compared with its substrate-bound counterpart, several significant structural rearrangements can be observed. Some rearrangements correspond to those previously reported by Gatzeva-Topalova and coworkers, some could not be observed by comparison with the structures of the isolated ArnA DH and TF domains and, most interestingly, several rearrangements are obviously involved in the mechanism conferring cooperativity to the ArnA dehydrogenase activity, a feature that had previously been reported by the Wood group (Polizzi *et al.*, 2012). Finally, the most striking feature of our apo ArnA crystal structure is the presence of a deep and narrow pocket at the centre of each propeller occupied by a DTT molecule, while only a shallow depression is observed at the corresponding position in the substrate-bound structure. Based on these results and our apo full-length crystal structure, we postulate a small effector molecule that binds to the central pocket and presumably regulates the catalytic properties of ArnA.

2. Materials and methods

2.1. Protein expression and purification

Escherichia coli strain Rosetta2 BL21(DE3) was transformed with expression vector pETM11 carrying a mammalian gene sequence. After induction of heterologous protein expression with 0.5 m*M* IPTG, the culture was grown with vigorous shaking for 12 h at 15°C. The cells were harvested by centrifugation and lysed by sonication. ArnA was fortuitously co-purified with the mammalian hexahistidine-tagged target protein on an Ni–NTA column (Quiagen, Hilden, Germany). To separate ArnA from the heterologously expressed target protein, the Ni–NTA eluate was dialyzed against buffer *A* (50 m*M* NaCl, 50 m*M* HEPES pH 7.5, 2 m*M* DTT) and loaded onto a Resource Q column (GE Healthcare, Munich, Germany). The column was eluted with a linear gradient to buffer *B* (1 *M* NaCl, 50 m*M* HEPES pH 7.5, 2 m*M* DTT) and almost pure ArnA appeared within an early peak at roughly 10% buffer *B*, well separated from the mammalian target protein, which eluted at roughly 30% buffer *B*. Fractions containing the ArnA protein were collected and concentrated by ultrafiltration in a Centricon membrane unit (Merck KGaA, Darmstadt, Germany). Finally, the ArnA protein was polished on a Superdex 200 10/300 size-exclusion column (GE Healthcare, Munich, Germany) equilibrated with buffer *A*, from which it eluted in a single Gaussian peak at a 10 ml delay volume. The ArnA-containing fractions were pooled, concentrated to 10 mg ml^{-1} and flash-cooled in liquid nitrogen for storage. The identity of the ArnA preparation was confirmed by peptide mass fingerprinting.

2.2. Crystallization, data collection and structure determination

ArnA was screened for crystallization using a random sparse-matrix screen by the hanging-drop method. Drops were produced by mixing 1 µl protein solution with 1 µl reservoir solution. After incubation at 16°C for 10 d, crystals of different shapes appeared under conditions containing either high-molecular-weight PEGs or pentaerythrytol propoxylate in the pH range 6.0–7.0. Testing on a synchrotron beamline revealed that only crystals grown with 10% PEG 8000, 0.2 *M* magnesium acetate, 0.1 *M* MOPS pH 6.5 as a reservoir solution

Table 1
Data collection and processing.

Values in parentheses are for the outer shell.

Radiation source	Beamline ID23-1, ESRF Grenoble
Wavelength (Å)	0.97661
Temperature (K)	100
Detector	PILATUS 6M
Crystal-to-detector distance (mm)	532
Rotation range per image (°)	0.15
Total rotation range (°)	180
Exposure time per image (s)	0.3
Space group	*P*1
a, *b*, *c* (Å)	106.7, 112.8, 113.6
α, β, γ (°)	81.9, 82.9, 83.8
Mosaicity (°)	0.12
Resolution range (Å)	50–2.7 (2.8–2.7)
Total No. of reflections	311621 (31552)
No. of unique reflections	138756 (13948)
Completeness (%)	97.5 (97.1)
Multiplicity	2.2 (2.3)
$\langle I/\sigma(I)\rangle$	9.9 (1.2)
$R_{\rm merge}$	0.047 (0.720)
$R_{\rm meas}$	0.061 (0.765)
Overall *B* factor from Wilson plot (Å^2)	76.8

Table 2
Structure solution and refinement.

Values in parentheses are for the outer shell.

Resolution range (Å)	50–2.7 (2.8–2.7)
No. of reflections, working set	131772
No. of reflections, test set	6967
Final $R_{\rm cryst}$	0.205 (0.357)
Final $R_{\rm free}$	0.232 (0.378)
No. of non-H atoms	
Protein	30190
Ligands	40
Water	9
Total	30239
R.m.s. deviations	
Bonds (Å)	0.005
Angles (°)	1.1
Average *B* factors (Å^2)	
Protein	61.1
Ligands	44.2
Water	14.3
Ramachandran plot	
Most favoured (%)	98.0
Disallowed residues	6 [His9 of chains *A*, *B*, *C*, *D*, *E* and *F*]
PDB code	4wkg

exhibited sufficient diffraction for structure determination. For data collection, such a crystal was transferred to reservoir solution supplemented with 30% glycerol and flash-cooled in a nylon loop with liquid nitrogen. The crystal was mounted in a 100 K nitrogen-gas stream and a data set was collected over 180° of rotation on beamline ID23-1 at ESRF Grenoble. The crystals belonged to space group *P*1, with unit-cell parameters $a = 106.7$, $b = 112.8$, $c = 113.6$ Å, $\alpha = 81.9$, $\beta = 83.0$, $\gamma = 83.8°$ and contained a single ArnA hexamer per unit cell. The data set was processed with *XDS* (Kabsch, 2010) and molecular replacement was performed with *Phaser* (McCoy *et al.*, 2007) using the coordinates of hexameric, substrate-bound ArnA (PDB entry 1z7e; Gatzeva-Topalova *et al.*, 2005*b*) as a search model. A single distinct solution was found and subjected to refinement with *phenix.refine* (Adams *et al.*, 2010). Model regions with significant structural rearrangements were then manually rebuilt within *Coot* (Emsley *et al.*, 2010) using model maps that were *B*-factor sharpened by −45 Å^2. After three further rounds of manual rebuilding and automated refinement as well as the addition of two DTT molecules, two acetate ions and nine water molecules, the $R_{\rm cryst}/R_{\rm free}$ factors converged and a model with excellent geometry and stereochemistry was obtained. The placement of waters was carried out manually. Up to two waters were built in each protomer at the most significant peaks within both the $F_{\rm obs} - F_{\rm calc}$ and the $2F_{\rm obs} - F_{\rm calc}$ density maps. Furthermore, waters were only built at positions that were likewise occupied by a water in the corresponding high-resolution structures of the isolated DH (Gatzeva-Topalova *et al.*, 2004) and TF (Gatzeva-Topalova *et al.*, 2005*a*) domains.

The Ramachandran plot indicates that residue His9 of chains *A*, *B*, *C*, *D*, *E* and *F* is situated on the border of the disallowed region. However, each of these residues features clear and unambiguous electron density and a good fit of the model to the density at this position. Moreover, the high-resolution structure of the isolated TF domain (Gatzeva-Topalova *et al.*, 2005*a*) shows His9 in a similar conformation. We thus conclude that His9 is in a strained conformation and therefore is a true Ramachandran outlier. The data-collection statistics are summarized in Table 1 and the model-refinement statistics in Table 2. Protein model figures were generated with *PyMOL* (Schrödinger, New York, USA).

3. Results and discussion

3.1. Overall structure of apo ArnA

Natively expressed ArnA from *E. coli* was purified by Ni–NTA metal-chelate affinity chromatography and gel filtration. Three different crystal forms were obtained in an extensive random sparse-matrix crystallization screen. However, only crystals grown in PEG/lithium citrate and belonging to space group *P*1 diffracted to a resolution of 2.7 Å suitable for structure determination. Their structure was solved by molecular replacement with the coordinates of UDP-GlcA/ATP-bound ArnA (Gatzeva-Topalova *et al.*, 2005*b*) and was refined to an $R_{\rm cryst}$ and $R_{\rm free}$ of 20.5 and 23.2%, respectively (see Table 1 for data-collection statistics and Table 2 for model-refinement statistics). The asymmetric unit harbours six chains of the ArnA protein arranged in the same hexameric oligomerization scheme as observed for the structure of substrate-bound full-length ArnA (Gatzeva-Topalova *et al.*, 2005*b*). Likewise, the apo ArnA hexamer is organized as a dimer of trimers. A single trimer appears as a three-bladed propeller with a pore along the propeller axis. The three DH domains are situated at the propeller centre next to the threefold symmetry axis and the three TF domains are situated at the propeller periphery (Fig. 2*a*, coloured chains). The second trimer (Fig. 2*a*, grey chains) is related to the first by a twofold axis perpendicular to the threefold of the trimer. Both trimers share an extended contact surface. Strikingly, the apo ArnA crystal structure reveals that the respective propeller

structure of its two trimers is tighter, having its dehydrogenase domains positioned closer to the threefold axis of the trimer compared with the situation in the crystal structure of substrate-bound ArnA.

3.2. Structural rearrangements trigger the formation of a central pocket in apo ArnA

A closer inspection of the apo ArnA crystal structure revealed several sites with significant conformational differences within the DH domain in comparison to the structure of substrate-bound ArnA. The largest structural rearrangement is observed for residues 500–509. In apo ArnA, they form a loop that occupies the NAD^+-binding site. In the substrate-bound structure, residues 500–505 form a helix that directly contacts and thereby entraps the bound nucleotide cofactor. This structural change had already been noticed by comparison with the isolated DH domain (Gatzeva-Topalova *et al.*, 2005*b*). However, several other significant changes present in the apo ArnA crystal structure cannot be observed in the isolated DH domain. Most strikingly, residues Trp375 and His372 located in the pore at the centre of each of the two trimeric propellers line a narrow and deep pocket (Fig. 3*b*) harbouring significant additional electron density. These two positions with extra density could each be fitted by a DTT molecule in two alternative conformations (Fig. 2*c* and Supplementary Fig. S1) that were both assigned with an occupancy of 0.5. The overall *B* factors of both conformations refine to similar values. This finding is remarkable, as in the substrate-bound ArnA structure the pore at the centre of the propeller ends in a shallow depression (Fig. 3*a*). In detail, the following structural rearrangements that contribute to the formation of the central pocket are observed in the DH domain around the pore. The description refers to the trimer comprising chains *D*, *E* and *F* (coloured green, purple and magenta, respectively, throughout Figs. 2 and 3) and to the transition of substrate-bound ArnA to apo ArnA. If no chain identifier is specified, the descriptions apply equally to all three chains of the trimer. See Figs. 3(*c*) and 3(*d*) for a superposition of the structures of substrate-bound ArnA with apo ArnA and Fig. 4(*a*) for a heat map of the conformational changes in the context of intersubunit contacts.

(i) The three subunits of the trimer move closer to the threefold symmetry axis (Figs. 3*a*, 3*b* and 3*c*). This overall conformational change is closely linked to the local changes described below.

(ii) Helix 373–381 rotates roughly 14° around its C-terminal end, which effects a significant repositioning of the residues around its N-terminal end, in particular His372 (Figs. 3*c* and 3*d*). The closely neighbouring C-terminal end of strand 362–367 is affected by a similar movement (Fig. 4*a*). These changes have a strong impact on the trimer interface of the DH domain.

(iii) In the substrate-bound form, χ_1 of Trp375 is in a *trans* conformation, resulting in a radial orientation of the indole ring system with respect to the the central cavity (Fig. 3*a*). Upon substrate binding, its indole ring moves inwards and rearranges into a tangential orientation (Figs. 3*a*, 3*b* and 3*c*). Remarkably, the underlying conformational change is different between Trp375(*F*) on one side and Trp375(*D*) and Trp375(*E*) on the other side (Fig. 3*d*). This phenomenon causes an asymmetric appearance of the apo ArnA central pocket (Figs. 3*b* and 3*c*). During substrate binding, the χ_1 angles of both Trp375(*D*) and Trp375(*E*) stay in a *trans* conformation and react mainly by a rotation of roughly 40° around their χ_2 angles. In contrast, χ_1 of Trp375(*F*) moves from a *trans* to a *gauche* minus conformation, while its χ_2 angle remains mostly unchanged.

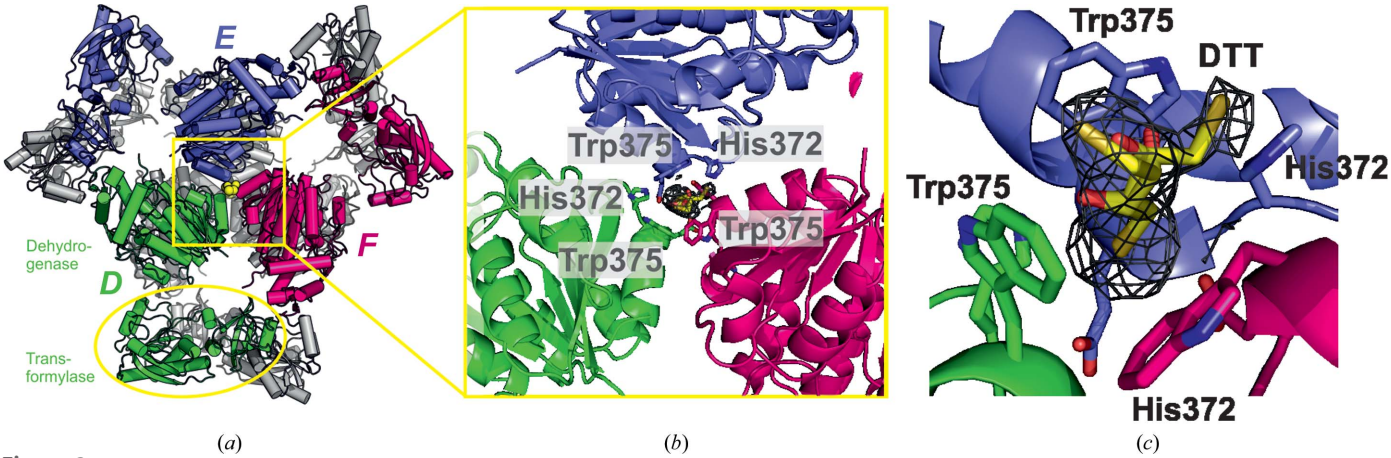

(*a*) (*b*) (*c*)

Figure 2
Crystal structure of full-length apo ArnA. (*a*) Overall view along the threefold axis of the trimer. The protomers of the first trimer in the foreground are coloured according to the chain; the protomers of the second trimer in the background are coloured grey. The bound DTT molecule is shown as yellow balls. For clarity, only one of the two alternative conformations is shown for the DTT ligand. (*b*) Enlargement of the region of the central binding pocket; the DTT molecule is shown as a stick model. The cage represents the 0.8σ contour of the simulated-annealing OMIT map for the bound DTT molecule. Both alternative conformations are shown for the DTT ligand. (*c*) Further enlargement of the view in (*b*); for clarity, the view is slightly tilted. Both alternative conformations are shown for the DTT ligand. The colouring scheme throughout the three panels is as follows. C atoms: purple, chain *E*; green, chain *D*; magenta, chain *F*; yellow, DTT ligand. All other atom types are coloured according to the CPK scheme. See also Supplementary Fig. S1 for a stereoview of the fitted DTT ligand in its two alternative conformations.

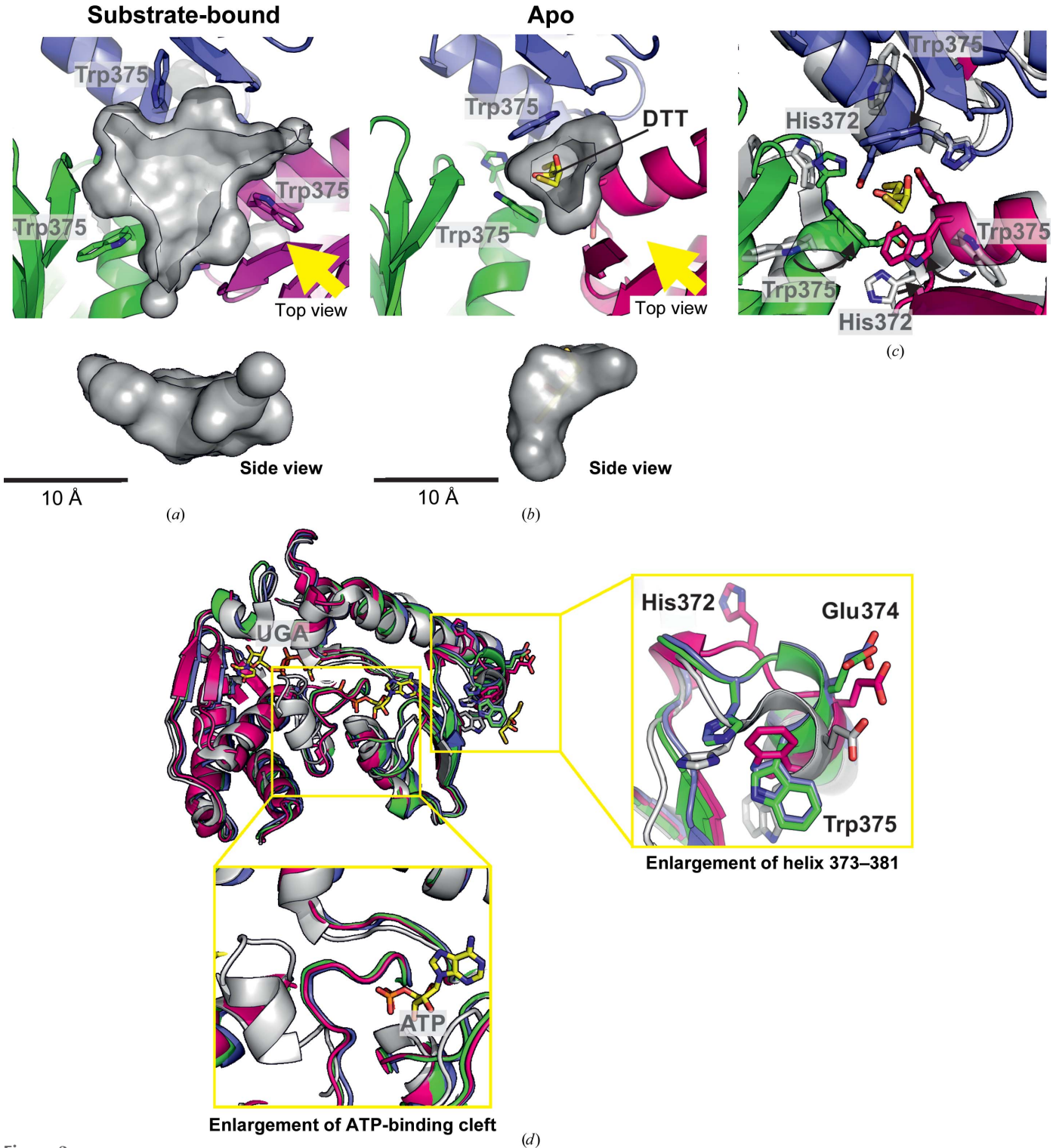

Figure 3
Molecular determinants that lead to the formation of the central binding pocket. For clarity, the DTT ligand is shown in only one of its two alternative conformations. (*a*) View of the area of the binding pocket for the situation in the substrate-bound crystal structure. The solvent-accessible surface of the cavity is presented in grey. Below: side view of the solvent-accessible surface of the cavity. The yellow arrow in the upper panel indicates the view direction for the side view shown below. The colour coding is similar to that in Fig. 2. (*b*) The same view as in (*a*) for the apo ArnA structure. The solvent-accessible surface of the cavity is presented in grey. Below: side view of the solvent-accessible surface of the cavity. The yellow arrow in the upper panel indicates the view direction for the side view shown below. The colour coding is similar to that in Fig. 2. (*c*) Superposition of the apo ArnA structure [colour coding as in (*b*)] with the substrate-bound structure (transparent grey) to illustrate the conformational changes induced by substrate binding/release (indicated by arrows). (*d*) Superposition of the three chains of the first trimer of the apo ArnA structure with the substrate-bound crystal structure of the dehydrogenase domain. The colour coding is according to (*c*). The bound ATP and UGA molecules are shown in yellow (for C atoms; other atoms are in CPK colouring). Yellow boxes indicate enlarged views. This figure illustrates the different conformations found in the different protomers of apo ArnA in comparison to the substrate-bound structure shown in grey (only a single chain is shown).

(iv) As a consequence of the asymmetric change of χ_1 of Trp375(*F*) to the *gauche* minus conformation, the neighbouring His372(*F*) residue evades a clash by a rotation of roughly 120° that has its pivot point roughly at the position of the C^{α} atom. His372(*F*) therefore lines the deeper parts of the central pocket (Figs. 3*c* and 3*d*).

(v) Owing to the movement resulting from the tilt of helix 373–381 combined with a slight reorientation of Glu374, the latter moves inwards, lining the bottom of the central apo ArnA pocket (Fig. 3*c* and 3*d*).

Similar observations are made for the second trimer comprising chains *A*, *B* and *C* (coloured grey in Fig. 2*a*). In sum, these conformational changes enable the formation of the observed pocket in apo ArnA. Of note, the overlay of the two conformations of the bound DTT molecule yields a slightly asymmetric shape that fills the asymmetric pocket much better than a DTT molecule in a single conformation. As the observed rearrangements are obviously elicited by binding of the ArnA(DH) substrate molecules, we moved on to define the structural determinants that sense the presence of substrate molecules and transfer the corresponding signal to the pore region.

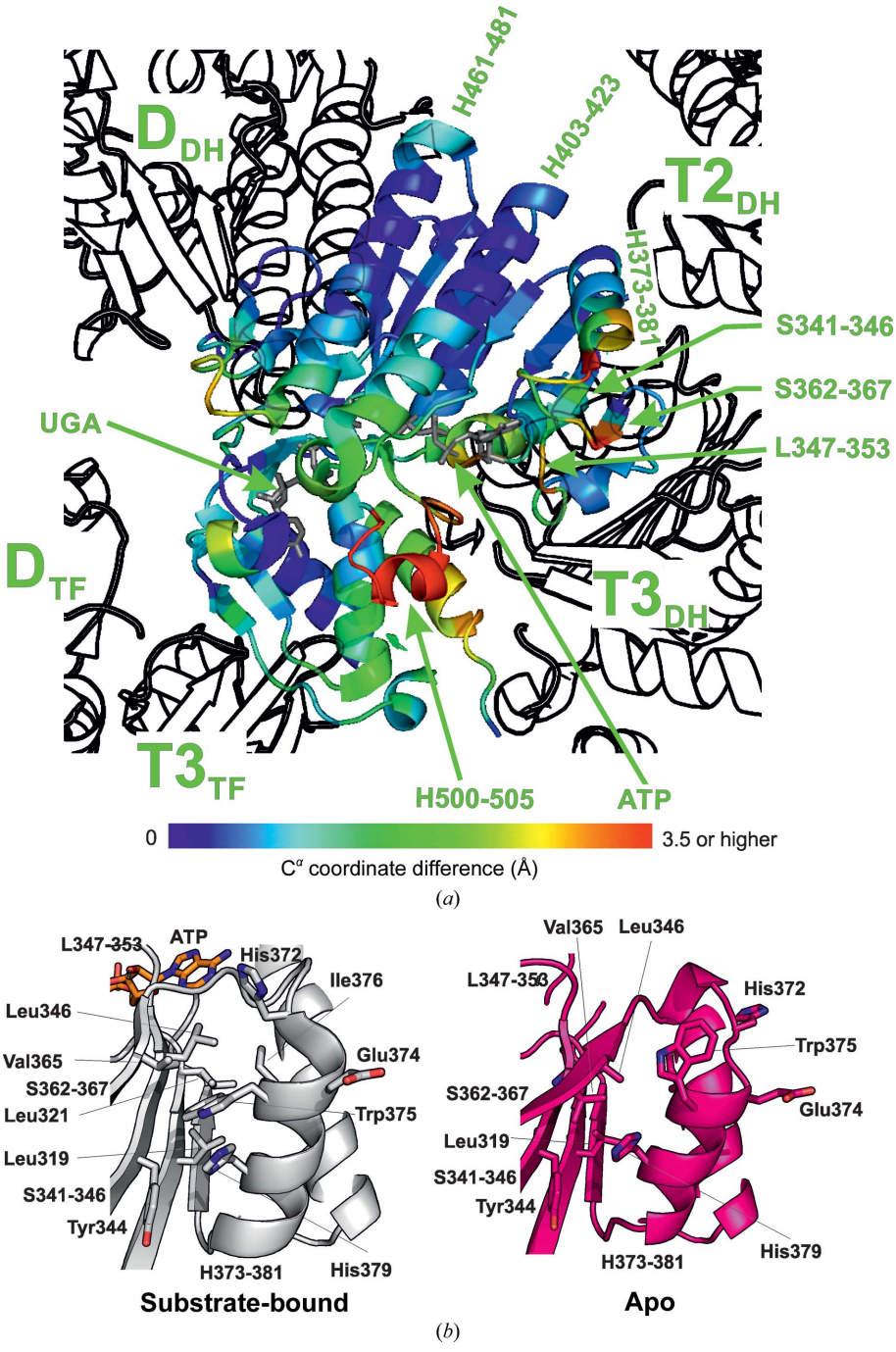

Figure 4
Conformational differences between the apo ArnA structure and the structure of substrate-bound ArnA. (*a*) Heat map of coordinate C^{α} differences of the apo ArnA structure from the ArnA–UGA–ATP complex (PDB entry 1z7e; Gatzeva-Topalova *et al.*, 2005*b*). The superposition was calculated for the C^{α} positions of the respective DH domains. The differences are colour-coded and mapped onto the model of the substrate-bound ArnA structure. The bound UGA and ATP molecules are shown in grey. The neighbouring protomers are depicted as grey outlines (D_{DH}, dimer-related dehydrogenase domain; D_{TF}, dimer-related transformylase domain; Tn_{DH}, trimer-related dehydrogenase domain; Tn_{TF}, trimer-related transformylase domain). (*b*) Details of the hydrophobic pocket P1 that harbours Trp375 in the substrate-bound ArnA structure. Colour coding is as in Fig. 3(*d*); the situation in the substrate-bound ArnA structure is shown on the left and the situation in the apo ArnA structure is shown on the right.

3.3. Communication of the dehydrogenase domain substrate-binding site with the central pocket

To find the origin of the signal generated by the bound substrates and to elucidate the mechanism by which it is transferred, we examined the region around the two substrate-binding clefts for particularly strong deviations between the apo and the substrate-bound ArnA structures (Fig. 4*a*). As mentioned earlier, the most prominent coordinate differences are observed in loop 500–509 that rearranges into helix 500–505 in the substrate-bound state. However, these residues are strongly solvent-exposed and are not involved in extensive interaction with other parts of the domain or neighbouring protomers. Therefore, it is unlikely that they contribute directly to the signal in question or its propagation. A similar situation is seen for loop 605–616. It is disordered in the apo structure and folds into a one-turn helix that contacts the uracil ring of UGA in the substrate-

bound structure. This structural element is also unlikely to contribute to the generation or propagation of the signal for the reasons mentioned above. Strikingly, all other significant rearrangements occur next to the adenine base of the nucleotide coenzyme, which is located in the close vicinity of the central pore of the trimer and the trimeric contact surfaces of the DH domain. When examining this area, we found that the signal in question is evidently generated and transduced by a cascade of molecular rearrangements which are described as follows for the transition of substrate-bound ArnA to apo ArnA (residue names and names of the secondary-structure elements without chain identifiers refer to the respective residues of all three chains of the trimer).

(i) Upon cofactor binding, loop 347–353 and the C-terminal end of strand β341–346 move towards the adenine moiety of the ATP molecule (Fig. 4*a*). This enables the side chain of Ile348 to establish van der Waals interactions with the adenine ring in the substrate-bound structure. The observed shift amounts to a maximum of 2.4 Å at the C^{α} atom of Gly349.

(ii) The movement described in (i) also embraces the neighbouring strand β362–366 and peaks at its C-terminal end, where the C^{α} atom of Glu366 is shifted by 2.9 Å (Fig. 4*a*).

(iii) Val365 located at the C-terminal end of strand β362–366 lines a hydrophobic pocket (which we will refer to as pocket P1) that harbours Trp375 in the substrate-bound structure (Fig. 4*b*, left panel). In the apo structure Trp375 has been fully displaced out of pocket P1 owing to the movement described in (ii) and Val365 has advanced into pocket P1, which has therefore collapsed (Fig. 4*b*, right panel; see also Fig. 3 for the role of Trp375 in the context of the central binding pocket).

(iv) The opposing side of pocket P1 is formed by His379 which, during the collapse of P1, also advances further into this pocket (Fig. 4*b*). Finally, in apo ArnA the C-terminal end of helix 373–381 has also moved into the space freed up by the collapse of pocket P1.

These four events eventually lead to the tilt of helix 373–381, the compaction of the apo ArnA trimer arrangement towards the threefold axis and the repositioning of its three Trp375 residues and some neighbouring residues which jointly facilitate the formation of the central pocket. In addition, a small and more generalized movement embraces the two dehydrogenase subdomains in a hinge motion and lets the enzyme compact around the bound substrates. This motion, previously observed by Gatzeva-Topalova and coworkers by comparison of substrate-bound ArnA with the isolated apo DH domain (Gatzeva-Topalova *et al.*, 2005*b*), contributes to an increase in the relative tilt of the two trimer interfaces of each protomer. By doing so, it adds to the less compact arrangement of the three protomers in each of the two trimers of the substrate-bound ArnA structure.

As the binding or release of the nucleotide coenzyme seems to be strictly linked *via* the aforementioned cascade of conformational changes to the formation or disturbance of the central pocket, it stands to reason that the signal cascade can also be controlled in the opposite way. We therefore postulate the existence of a small-molecule effector that is able to bind to the central pocket of ArnA and thus modulate its enzymatic properties. This hypothesis is supported by the fact that the pocket is occupied by a DTT molecule in the apo structure, possibly mimicking some interactions of the putative native ligand, even though it is virtually impossible that DTT is the native effector molecule in question. What could the mode of action of the postulated effector molecule be? One piece of the puzzle might be a catalytic shunt recently discovered by the Wood group by comparison of the ArnA DH domain with its human orthologue UDP-α-D-xylose synthase (hUXS; Eixelsberger *et al.*, 2012). Some structural elements that constitute the shunt are conserved among both enzymes (Polizzi *et al.*, 2012), while in particular a loop (residues 120–124; hUXS numbering) that encloses the adenine moiety of the bound NAD^+ is shortened to a simple turn in ArnA (residues 348–349; ArnA numbering; Fig. 5). The absence of this element in ArnA might explain the preference of ArnA for the release of NADH and UX4O owing to less stringent binding of the coenzyme. In contrast, in hUXS the comparably tight binding of NADH/NAD^+ shunts the reaction towards the production of UDP-α-D-xylose, as the reduced nucleotide cofactor remains permanently bound to the enzyme and the reducing equivalents transferred onto the cofactor in the first reaction step are subsequently relocated to the substrate (Fig. 1*b*). While the enzymatic shunt is static in hUXS, it might conceivably be under the control of the small-molecule effector in question in ArnA. A putative effector molecule bound to the central pocket of ArnA that forces key residues of the signal transduction cascade such as Trp375 into a conformation close to that seen in the substrate-bound crystal structure may therefore inhibit the release of NADH. Hence, the shunt would by this means be influenced towards the catalytic preference observed for hUXS (compare Fig. 1).

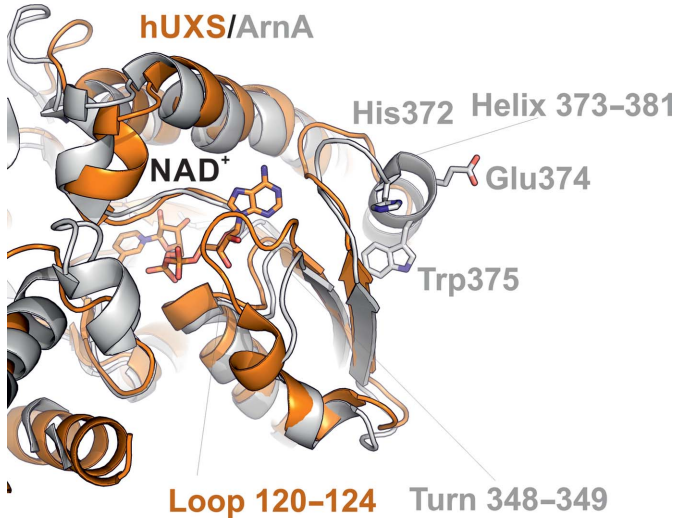

Figure 5
Superposition of the dehydrogenase domain of substrate-bound ArnA (grey) with human UDP-α-D-xylose synthase (hUXS): view of the area of the bound coenzyme (shown as in the hUXS structure).

3.4. Structural basis of intersubunit communication and enzymatic cooperativity

The ArnA substrate saturation curve exhibits a pronounced cooperativity for NAD^+, with a Hill coefficient of 1.7 and almost no cooperativity for UGA (Polizzi *et al.*, 2012). We thus examined the full-length ArnA crystal structure annotated with conformational differences between the apo and the substrate-bound forms (Fig. 4*a*) for mechanisms that could transfer the signal evoked by binding of NAD^+ onto neighbouring protomers and thereby cause the observed cooperative effect.

As the two protomers of the dimeric hUXS enzyme feature a common interface that is closely related to the dimeric interface observed in ArnA, and hUXS likewise displays significant cooperativity in its nucleotide cofactor-binding behaviour (Polizzi *et al.*, 2012), it appears likely that this interface at least contributes to the overall cooperativity detected for the ArnA NAD^+ binding. We therefore first turned to the dimer-type contacts within the ArnA hexamer. Here, distinct rearrangements are seen for the N-terminal ends of helix 461–481 and helix 403–423, and in particular for the loop preceding helix 461–481 (Fig. 4*a*). The majority of the dimeric contact surface on the DH domain is built up by these two helices contacting their dimer-related counterparts. In this way, the observed movements are easily transferred onto the dimer-related protomer. The most likely mechanism by which influence on the binding behaviour is finally exerted is the aforementioned hinge motion of the DH subdomains around the substrate-binding left.

We next turned to the trimeric DH domain contacts. It is obvious that the location of the adenine moiety of the bound NAD^+ in the close vicinity of the central pore of the ArnA trimer and therefore also the subunit interfaces of the trimer (Fig. 4*a*, compare with Fig. 3*d*) is well suited to communicate the signal to the neighbouring protomers. Concretely, the most evident place of signal transfer is the N-terminal end of helix 373–381, as it is one of the hotspots of conformational change and is directly involved in the contact with the same helix of the two neighbouring protomers within the trimer. Likewise, the C-terminal end of strand 362–367 contacts helix 373–381 of the neighbouring trimer-related protomer. This structural element was also identified as a centre of major structural rearrangements (Fig. 4*a*). Furthermore, as many interactions between neighbouring subunits of the trimer are found within the central binding pocket, the formation or destruction of this pocket is likely to be an important component of the mechanism that transfers the signal from the bound nucleotide cofactor to the neighbouring protomers.

3.5. Functional and structural analogies to haemoglobin and conclusion

The oxygen-binding behaviour of haemoglobin is widely regarded as the prototypical model system for a cooperative effect as well as for the principle of allosteric regulation. Hence, it is fascinating that haemoglobin has significant architectural and mechanistic similarity to ArnA in this regard, while there is no phylogenetic or functional relationship at all. Stunningly, the structure of heterotetrameric ($\alpha_2\beta_2$) deoxyhaemoglobin (Bolton & Perutz, 1970) likewise features a central binding site formed by two β subunits that collectively bind the allosteric effector 2,3-bisphosphoglycerate (2,3-BPG). Similar to the situation in ArnA, the site is not present in the structure of oxygenated haemoglobin. The X-ray structure of deoxyhaemoglobin bound to 2,3-BPG, which was first solved by Arnone (Arnone, 1972; Richard *et al.*, 1993), is able to explain the reduced oxygen affinity of the 2,3-BPG–deoxyhaemoglobin complex by the observed stabilization of the oxygen-free 'tight' form of haemoglobin (Supplementary Fig. S2). A further remarkable parallel of the 2,3-BPG–deoxyhaemoglobin structure to our apo ArnA structure is the breakage of the oligomeric symmetry in the side chains lining the effector-binding pocket (Arnone, 1972). In conclusion, by comparison to its substrate-bound counterpart and the crystal structure of hUXS, our model of apo ArnA provides a probable mechanistic explanation of the previously observed catalytic properties of the ArnA dehydrogenase functionality. Furthermore, the observed rearrangements might be important contributors to the mechanism of the catalytic shunt proposed previously by the Wood group. Finally, the existence of the central binding pocket occupied by a crystallographically well defined DTT molecule is a possible indication that the catalytic shunt observed in the ArnA DH domain might be under the allosteric control of an as yet to be identified small-molecule effector. As allosteric sites are potentially attractive targets for drug development (Csermely *et al.*, 2013; Grant *et al.*, 2011), the postulated allosteric effector is likely to be of future pharmaceutical relevance in the therapy of MDR infections, either as a novel drug lead or as a drug compound itself.

Acknowledgements

We thank Dr Bhupesh Prusty and Professor Dr Andreas Schlosser for performing the peptide mass-fingerprinting analysis. We thank the team at beamline ID23-1 of the European Synchrotron Radiation Facility (ESRF) in Grenoble, France for their excellent support during data collection. This work was supported by grants from the DFG to UF and CG (FI 573/7-1) and the Rudolf Virchow Centre Würzburg.

References

Adams, P. D. *et al.* (2010). *Acta Cryst.* D**66**, 213–221.
Arnone, A. (1972). *Nature (London)*, **237**, 146–149.
Bolton, W. & Perutz, M. F. (1970). *Nature (London)*, **228**, 551–552.
Breazeale, S. D., Ribeiro, A. A., McClerren, A. L. & Raetz, C. R. (2005). *J. Biol. Chem.* **280**, 14154–14167.
Breazeale, S. D., Ribeiro, A. A. & Raetz, C. R. (2002). *J. Biol. Chem.* **277**, 2886–2896.
Breazeale, S. D., Ribeiro, A. A. & Raetz, C. R. (2003). *J. Biol. Chem.* **278**, 24731–24739.
Chen, Y.-Y., Ko, T.-P., Lin, C.-H., Chen, W.-H. & Wang, A. H.-J. (2011). *J. Struct. Biol.* **175**, 300–310.
Csermely, P., Nussinov, R. & Szilágyi, A. (2013). *Curr. Top. Med. Chem.* **13**, 2–4.

Eixelsberger, T., Sykora, S., Egger, S., Brunsteiner, M., Kavanagh, K. L., Oppermann, U., Brecker, L. & Nidetzky, B. (2012). *J. Biol. Chem.* **287**, 31349–31358.
Emsley, P., Lohkamp, B., Scott, W. G. & Cowtan, K. (2010). *Acta Cryst.* D**66**, 486–501.
Falagas, M. E., Rafailidis, P. I. & Matthaiou, D. K. (2010). *Drug Resist. Updat.* **13**, 132–138.
Gatzeva-Topalova, P. Z., May, A. P. & Sousa, M. C. (2004). *Biochemistry*, **43**, 13370–13379.
Gatzeva-Topalova, P. Z., May, A. P. & Sousa, M. C. (2005*a*). *Biochemistry*, **44**, 5328–5338.
Gatzeva-Topalova, P. Z., May, A. P. & Sousa, M. C. (2005*b*). *Structure*, **13**, 929–942.
Grant, B. J., Lukman, S., Hocker, H. J., Sayyah, J., Brown, J. H., McCammon, J. A. & Gorfe, A. A. (2011). *PLoS One*, **6**, e25711.
Gunn, J. S. (2001). *J. Endotoxin Res.* **7**, 57–62.
Gunn, J. S., Lim, K. B., Krueger, J., Kim, K., Guo, L., Hackett, M. & Miller, S. I. (1998). *Mol. Microbiol.* **27**, 1171–1182.
Gunn, J. S., Ryan, S. S., Van Velkinburgh, J. C., Ernst, R. K. & Miller, S. I. (2000). *Infect. Immun.* **68**, 6139–6146.
Guo, L., Lim, K. B., Gunn, J. S., Bainbridge, B., Darveau, R. P., Hackett, M. & Miller, S. I. (1997). *Science*, **276**, 250–253.
Hancock, R. E., Falla, T. & Brown, M. (1995). *Adv. Microb. Physiol.* **37**, 135–175.
Helander, I. M., Kilpeläinen, I. & Vaara, M. (1994). *Mol. Microbiol.* **11**, 481–487.
Kabsch, W. (2010). *Acta Cryst.* D**66**, 125–132.
Kallberg, Y., Oppermann, U. & Persson, B. (2010). *FEBS J.* **277**, 2375–2386.
Kavanagh, K. L., Jörnvall, H., Persson, B. & Oppermann, U. (2008). *Cell. Mol. Life Sci.* **65**, 3895–3906.
Lee, M. & Sousa, M. C. (2014). *Biochemistry*, **53**, 796–805.
Li, J., Nation, R. L., Turnidge, J. D., Milne, R. W., Coulthard, K., Rayner, C. R. & Paterson, D. L. (2006). *Lancet Infect. Dis.* **6**, 589–601.
Lounatmaa, K., Mäkelä, P. H. & Sarvas, M. (1976). *J. Bacteriol.* **127**, 1400–1407.
Lounatmaa, K. & Nanninga, N. (1976). *J. Bacteriol.* **128**, 665–667.
McCoy, A. J., Grosse-Kunstleve, R. W., Adams, P. D., Winn, M. D., Storoni, L. C. & Read, R. J. (2007). *J. Appl. Cryst.* **40**, 658–674.
Matsuzaki, K. (1999). *Biochim. Biophys. Acta*, **1462**, 1–10.
Moffatt, J. H., Harper, M., Harrison, P., Hale, J. D. F., Vinogradov, E., Seemann, T., Henry, R., Crane, B., St Michael, F., Cox, A. D., Adler, B., Nation, R. L., Li, J. & Boyce, J. D. (2010). *Antimicrob. Agents Chemother.* **54**, 4971–4977.
Noland, B. W., Newman, J. M., Hendle, J., Badger, J., Christopher, J. A., Tresser, J., Buchanan, M. D., Wright, T. A., Rutter, M. E., Sanderson, W. E., Müller-Dieckmann, H. J., Gajiwala, K. S. & Buchanan, S. G. (2002). *Structure*, **10**, 1569–1580.
Nummila, K., Kilpeläinen, I., Zähringer, U., Vaara, M. & Helander, I. M. (1995). *Mol. Microbiol.* **16**, 271–278.
Polizzi, S. J., Walsh, R. M. Jr, Peeples, W. B., Lim, J. M., Wells, L. & Wood, Z. A. (2012). *Biochemistry*, **51**, 8844–8855.
Reddy, K. V., Yedery, R. D. & Aranha, C. (2004). *Int. J. Antimicrob. Agents*, **24**, 536–547.
Richard, V., Dodson, G. G. & Mauguen, Y. (1993). *J. Mol. Biol.* **233**, 270–274.
Rocha, J., Popescu, A. O., Borges, P., Mil-Homens, D., Moreira, L. M., Sá-Correia, I., Fialho, A. M. & Frazão, C. (2011). *J. Bacteriol.* **193**, 3978–3987.
Shai, Y. (1999). *Biochim. Biophys. Acta*, **1462**, 55–70.
Trent, M. S., Ribeiro, A. A., Lin, S., Cotter, R. J. & Raetz, C. R. (2001). *J. Biol. Chem.* **276**, 43122–43131.
Vaara, M. (2013). *J. Antimicrob. Chemother.* **68**, 1213–1219.
Velkov, T., Thompson, P. E., Nation, R. L. & Li, J. (2010). *J. Med. Chem.* **53**, 1898–1916.
Yahav, D., Farbman, L., Leibovici, L. & Paul, M. (2012). *Clin. Microbiol. Infect.* **18**, 18–29.
Yang, L., Weiss, T. M., Lehrer, R. I. & Huang, H. W. (2000). *Biophys. J.* **79**, 2002–2009.
Zasloff, M. (2002). *Nature (London)* **415**, 389–395.
Zavascki, A. P., Goldani, L. Z., Li, J. & Nation, R. L. (2007). *J. Antimicrob. Chemother.* **60**, 1206–1215.
Zhou, Z., Ribeiro, A. A., Lin, S., Cotter, R. J., Miller, S. I. & Raetz, C. R. (2001). *J. Biol. Chem.* **276**, 43111–43121.